Supplementary Information for: Molecular Simulation of Structures and Mechanical Properties of Nanocomposite Networks Consisting of Disk-shaped Particles and Polymers

Tsutomu Furuya[a] and Tsuyoshi Koga*[a]

September 25, 2018

Results of Preliminary Simulation

Geometric Structure of Disk-shaped Particle

In order to investigate the geometric structure of the disk-shaped particle, we first calculate the average plane of each disk-shaped particles by fitting the positions of the beads to an equation of a plane $\mathbf{n}_i(t)\cdot[\mathbf{r}-\mathbf{r}_{\mathrm{cm},i}(t)]=0$. Here, $\mathbf{n}_i(t)$ is the unit normal vector of the average plane of the i-th disk-shaped particle; $\mathbf{r}$ is the position vector of a point on the plane; and $\mathbf{r}_{\mathrm{cm},i}(t)$ is the position vector of the center of mass of the i-th disk-shaped particle. The root mean square deviation σ_{rmsd} of the disk-shaped particle beads from the average plane is then calculated by the following equation:

$$\sigma_{\mathrm{rmsd}}=\sqrt{\left\langle\frac{1}{n_{\mathrm{d}}N_{\mathrm{d}}}\sum_{i=1}^{N_{\mathrm{d}}}\sum_{j=1}^{n_{\mathrm{d}}}\left\{\mathbf{n}_i(t)\cdot\left[\mathbf{r}_j(t)-\mathbf{r}_{\mathrm{cm},i}(t)\right]\right\}^2\right\rangle}. \tag{S1}$$

Here, $\mathbf{r}_j(t)$ is the position vector of the j-th beads belonging to the i-th disk-shaped particle. The average length l_{diag} of the diagonals of the disk-shaped particles is calculated as $l_{\mathrm{diag}}=\langle r_{\mathrm{v}}\rangle+\sigma_{\mathrm{LJ}}$. Here, $\langle r_{\mathrm{v}}\rangle$ is the average distance between the beads at the vertices, *e.g.*, A and B in the inset of Fig. S1. Figure S1 shows the spring constant k_θ dependences of the root mean deviation σ_{rmsd} of the disk-shaped particle beads and the average length l_{diag} of the diagonal. At $k_\theta=1500\varepsilon_{\mathrm{LJ}}$, the root mean deviation σ_{rmsd} is about $0.14\sigma_{\mathrm{LJ}}$ and the average length l_{diag} of the diagonal is about $4.84\sigma_{\mathrm{LJ}}$; therefore, we consider that the structures of the disk-shaped particles are well maintained. Since the equilibrium length of each bond is about $0.961\sigma_{\mathrm{LJ}}$, the average length l_{diag} of the diagonal becomes $4.84\sigma_{\mathrm{LJ}}$ when the disk-shaped particle beads constitute an ideal plane with the equilibrium bond length. With increasing the spring constant k_θ, the root mean deviation σ_{rmsd} slightly decreases, which is approximately proportional to $k_\theta^{-0.2}$. However, the average length l_{diag} of the diagonal exceeds $4.84\sigma_{\mathrm{LJ}}$. Hence, we set the spring constant at $k_\theta=1500\varepsilon_{\mathrm{LJ}}$ in this study. We confirmed that the elongation stress σ_{ue} at low strain and the tensile modulus E are almost independent of the spring constant k_θ at $1500\varepsilon_{\mathrm{LJ}}\leq k_\theta\leq 5000\varepsilon_{\mathrm{LJ}}$ (Fig. S2).

Time Development of Systems

Figure S3 shows the time developments of the average functionality $\langle g\rangle$ of the disk-shaped particles and the pressure. The results in Fig. S3 are the averages of five independent runs with the systems

[a] *Department of Polymer Chemistry, Graduate School of Engineering, Kyoto University, Katsura, Kyoto 615-8510, Japan. E-mail: tkoga@phys.polym.kyoto-u.ac.jp*

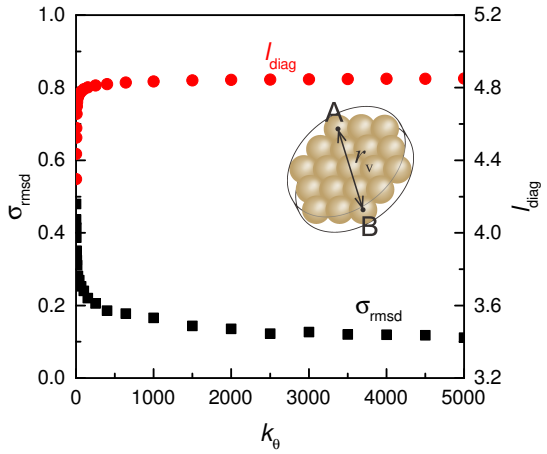

Figure S1 The spring constant k_θ dependences of the root mean deviation σ_{rmsd} of the disk-shaped particle beads from the average plane and the average length l_{diag} of the diagonals of the disk-shaped particles. The inset shows the schematic illustration of the distance r_{v} between the beads at the vertices.

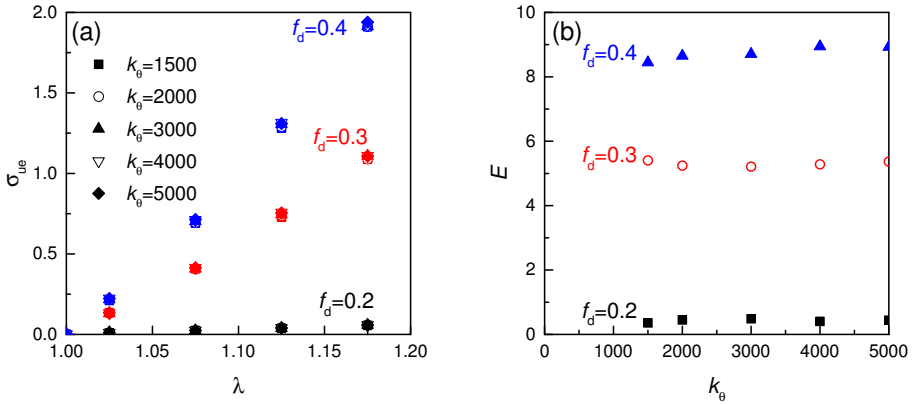

Figure S2 (a) The spring constant k_θ dependence of the elongation stress σ_{ue}. The spring constant k_θ is varied from data to data: $k_\theta = 1500\varepsilon_{\mathrm{LJ}}$ (■), $k_\theta = 2000\varepsilon_{\mathrm{LJ}}$ (◯), $k_\theta = 3000\varepsilon_{\mathrm{LJ}}$ (▲), $k_\theta = 4000\varepsilon_{\mathrm{LJ}}$ (▽), and $k_\theta = 5000\varepsilon_{\mathrm{LJ}}$ (♦). The polymer model is HP38. (b) The tensile modulus E shown as a function of the spring constant k_θ. The composition ratio f_{d} is varied from data to data: $f_{\mathrm{d}} = 0.2$ (■), $f_{\mathrm{d}} = 0.3$ (◯), and $f_{\mathrm{d}} = 0.4$ (▲). The polymer model is HP38.

of $n_t = 5.7 \times 10^3$. From Fig. S3, we find that the systems reach each steady state by $1.5 \times 10^5 \tau_{LJ}$ simulation. We then evaluate the steady state values from the average values at $1.5 \times 10^5 \tau_{LJ} < t \leq 2.5 \times 10^5 \tau_{LJ}$ (the dashed lines in Fig. S3). The average functionality $\langle g \rangle$ and the pressure rapidly approach each steady state value. After the calculation of $5 \times 10^4 \tau_{LJ}$ simulation, the deviation in the average functionality $\langle g \rangle$ becomes within 3% of the steady state value and the difference in the pressure from the steady state is less than 0.04. The pressure corresponds to $-\sigma_{diag}$, where σ_{diag} is the average of the diagonal components of the stress tensor. As shown in Fig. S13, the measurement range of the pressure is $-0.2 \lesssim -\sigma_{diag} \lesssim 1.5$; hence, the pressure difference 0.04 is less than 3% of the measurement range of the pressure. Therefore, we consider that the systems almost reach the equilibrium by $5 \times 10^4 \tau_{LJ}$ simulation. In order to reduce the calculation cost, we set the simulation times for the equilibration to $5 \times 10^4 \tau_{LJ}$. We confirmed that our simulation results, which correspond to the average values at $5 \times 10^4 \tau_{LJ} < t \leq 1 \times 10^5 \tau_{LJ}$, well agree with the steady state values (Fig. S4).

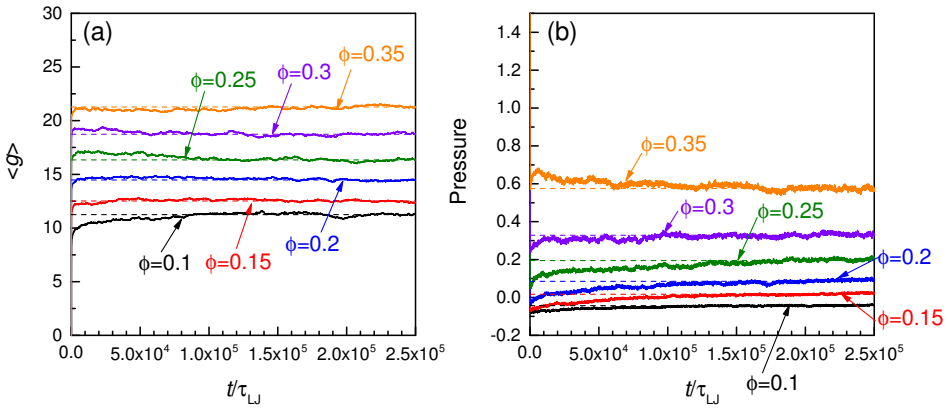

Figure S3 Time developments of (a) the average functionality $\langle g \rangle$ of the disk-shaped particles and (b) the pressure. The composition ratio f_d is fixed at $f_d = 0.4$ and the volume fraction ϕ is varied from data to data. For clarity, each pressure for $\phi > 0.1$ is shifted upward by increments of 0.1 in the pressure. The dashed lines indicate the steady state values. The polymer model is HP38.

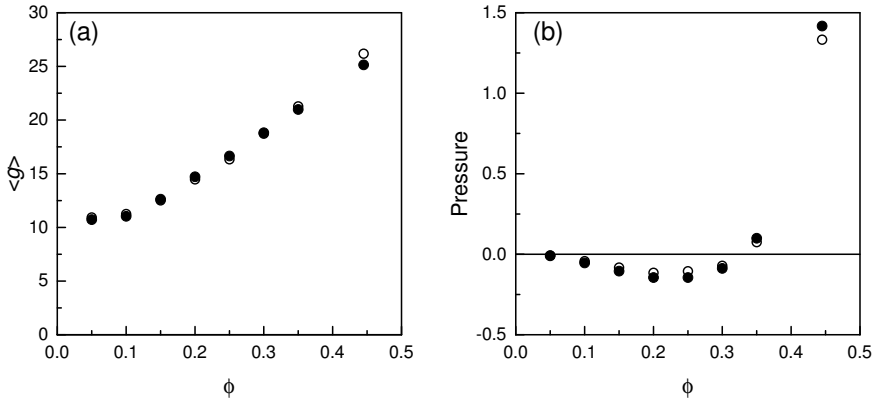

Figure S4 (a) The average functionality $\langle g \rangle$ of the disk-shaped particles and (b) the pressure shown as functions of the volume fraction ϕ. The filled symbols indicate the average values at $5 \times 10^4 \tau_{LJ} < t \leq 1 \times 10^5 \tau_{LJ}$ and the open symbols indicate the steady state values. The composition ratio f_d is fixed at $f_d = 0.4$ and the polymer model is HP38.

Relaxation Times of Polymer and Disk-shaped Particle and Average Lifetime of Physical Bond

In order to estimate the longest Rouse relaxation time $\tau_{\rm R}$ of the HP38 polymer and the rotational relaxation time $\tau_{\rm d}$ of the disk-shaped particle, we calculate the autocorrelation function $C_{\rm R}(t) \equiv \langle \mathbf{R}_i(t) \cdot \mathbf{R}_i(0) \rangle / \langle |\mathbf{R}_i(0)|^2 \rangle$ of the end-to-end vector of the polymer and the autocorrelation function $C_{\rm n}(t) \equiv \langle 3[\mathbf{n}_i(t) \cdot \mathbf{n}_i(0)]^2 - 1 \rangle / 2$ of the normal vector of the disk-shaped particle without the bond formation. Here, $\mathbf{R}_i(t)$ is the end-to-end vector of the i-th polymer at time t and $\mathbf{n}_i(t)$ is the unit normal vector of the i-th disk-shaped particle at time t. We then fit the autocorrelation functions $C_{\rm R}(t)$ and $C_{\rm n}(t)$ to exponentials $A_{\rm R} \exp(-t/\tau_{\rm R})$ and $A_{\rm d} \exp(-t/\tau_{\rm d})$, respectively. Figure S5 shows the autocorrelation functions. Figure S6 indicates the volume fraction ϕ dependences of the relaxation times $\tau_{\rm R}$ and $\tau_{\rm d}$. From Fig. S6, at the equilibrium swelling state ($0.13 \lesssim \phi \lesssim 0.33$), the relaxation times $\tau_{\rm R}$ and $\tau_{\rm d}$ are estimated to $1.8 \times 10^2 \tau_{\rm LJ} \lesssim \tau_{\rm R} \lesssim 5.0 \times 10^2 \tau_{\rm LJ}$ and $2.0 \times 10 \tau_{\rm LJ} \lesssim \tau_{\rm d} \lesssim 2.6 \times 10^2 \tau_{\rm LJ}$, respectively.

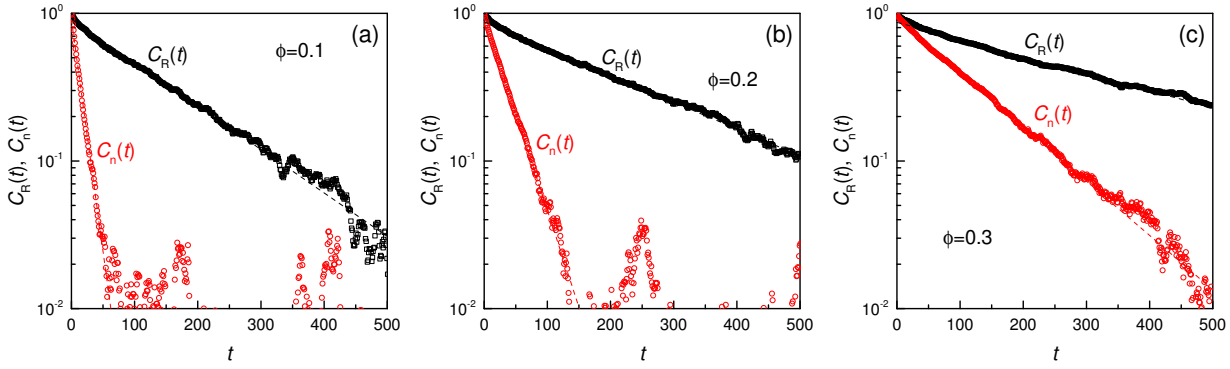

Figure S5 The autocorrelation functions $C_{\rm R}(t)$ and $C_{\rm n}(t)$ at (a) $\phi = 0.1$, (b) $\phi = 0.2$, and (c) $\phi = 0.3$. The composition ratio $f_{\rm d}$ is fixed at $f_{\rm d} = 0.5$. The dashed lines indicate the fitting results.

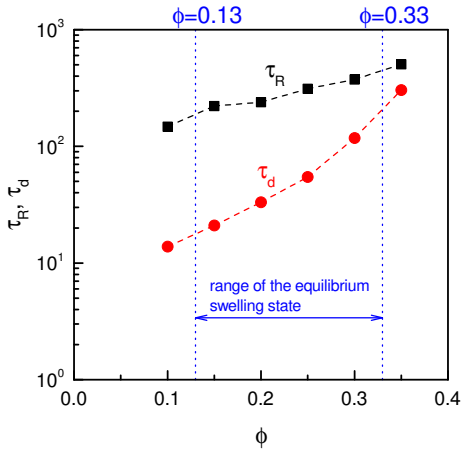

Figure S6 The relaxation times $\tau_{\rm R}$ and $\tau_{\rm d}$ shown as functions of the volume fraction ϕ. The composition ratio $f_{\rm d}$ is fixed at $f_{\rm d} = 0.5$.

In order to evaluate the lifetime $\tau_{\rm a}$ of the physical bonds, we monitor the frequency distribution $P_{\rm life}(t)$ of the breakages of the physical bonds after time t of the physical bond formation. Figure S7 shows the frequency distribution $P_{\rm life}(t)$. From the integral $\tau_{\rm a} = \int t P_{\rm life}(t) dt$, we find that the average lifetime $\tau_{\rm a}$ is $9 \times 10^3 \tau_{\rm LJ} \lesssim \tau_{\rm a} \lesssim 1 \times 10^4 \tau_{\rm LJ}$.

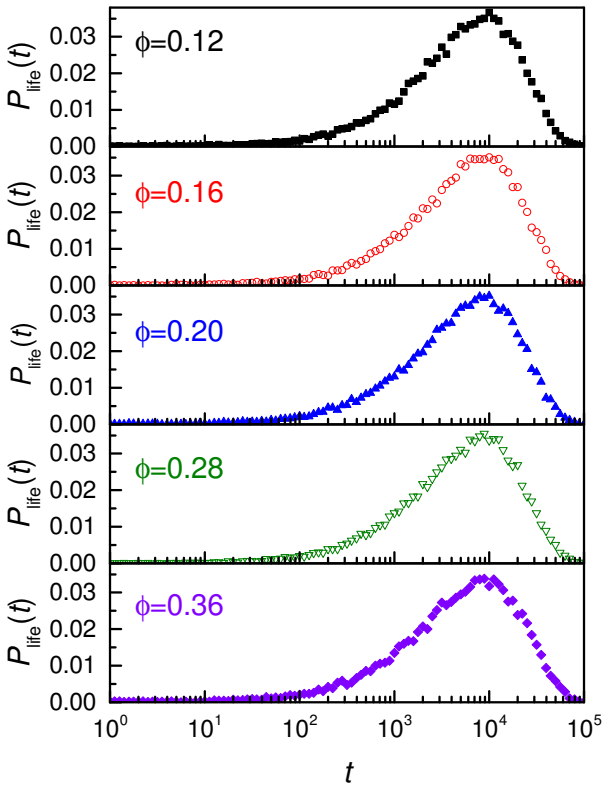

Figure S7 The frequency distribution $P_{\mathrm{life}}(t)$ of the breakages of the physical bonds after time t of the physical bond formation. The composition ratio f_{d} is fixed at $f_{\mathrm{d}} = 0.5$ and the polymer model is HP38.

Detailed Conditions of Simulation

Tables S1 and S2 shows the detailed conditions of the simulation.

Supplementary Data of Simulation

Classification of Polymer Chains

In order to analyze the structures of clusters consisting of the disk-shaped particles and the polymers, we classify parts of the polymer chains into the following five categories according to their adsorbing structures of the polymeric bonds: bridge chain, dangling chain, loop chain, train chain, and free chain (Fig. S8). The bridge chain indicates a part of a polymer which connects a pair of disk-shaped particles (the red lines in Fig. S8). The dangling chain is a part from an unadsorbed polymer end to the nearest adsorbed point along the polymer chain (the blue lines in Fig. S8). The loop chain corresponds an unadsorbed part between two adsorbed points (the green lines in Fig. S8). The train chain is a part in which two or more polymer beads are consecutively adsorbed on a disk-shaped particle (the black lines in Fig. S8). The free chain is an unadsorbed polymer (the violet lines in Fig. S8). Figure S9 shows the relative populations of each chain category as functions of the composition ratio f_{d} for the varying volume fraction ϕ. Here, the relative population is the ratio of the number of each chain category to the total number of all the chain categories. The relative population of the bridge chains sharply increases with increasing the composition ratio f_{d} at the relatively low composition ratios ($f_{\mathrm{d}} < 0.4$) and gradually increases at the relatively high composition ratios ($f_{\mathrm{d}} \geq 0.4$) (Fig. S9a). At the relatively low composition ratios ($f_{\mathrm{d}} < 0.4$), non-bridge chains composed of loop chains, dangling chains, train chains, and free chains exist at a certain level (Fig. S9b-e). The non-bridge chains do not contribute to the network formation; hence, we can say that the non-bridge chains delay the gelation of the systems at the relatively low composition ratios ($f_{\mathrm{d}} < 0.4$).

Table S1 The detailed conditions of the simulation to study the network structures.

polymer	f_d	N_p	N_d	ϕ	L^a
HP38 & MP38	0.1	135	30	$0.02 \sim 0.4$	$53.04 \sim 19.54$
HP38 & MP38	0.2	120	60	$0.02 \sim 0.4$	$53.04 \sim 19.54$
HP38 & MP38	0.3	105	90	$0.02 \sim 0.4$	$53.04 \sim 19.54$
HP38 & MP38	0.4	90	120	$0.02 \sim 0.4$	$53.04 \sim 19.54$
HP38 & MP38	0.5	75	150	$0.02 \sim 0.4$	$53.04 \sim 19.54$
HP38 & MP38	0.6	60	180	$0.02 \sim 0.4$	$53.04 \sim 19.54$
HP38 & MP38	0.7	45	210	$0.02 \sim 0.4$	$53.04 \sim 19.54$
HP38 & MP38	0.8	30	240	$0.02 \sim 0.4$	$53.04 \sim 19.54$
HP38 & MP38	0.9	15	270	$0.02 \sim 0.4$	$53.04 \sim 19.54$
HP19	0.1	270	30	$0.02 \sim 0.4$	$53.04 \sim 19.54$
HP19	0.2	240	60	$0.02 \sim 0.4$	$53.04 \sim 19.54$
HP19	0.3	210	90	$0.02 \sim 0.4$	$53.04 \sim 19.54$
HP19	0.4	180	120	$0.02 \sim 0.4$	$53.04 \sim 19.54$
HP19	0.5	150	150	$0.02 \sim 0.4$	$53.04 \sim 19.54$
HP19	0.6	120	180	$0.02 \sim 0.4$	$53.04 \sim 19.54$
HP19	0.7	90	210	$0.02 \sim 0.4$	$53.04 \sim 19.54$
HP19	0.8	60	240	$0.02 \sim 0.4$	$53.04 \sim 19.54$
HP19	0.9	30	270	$0.02 \sim 0.4$	$53.04 \sim 19.54$

[a] The length of a side of the simulation box.

Table S2 The detailed conditions of the simulation to study the stresses and the network structures under the uniaxial elongation.

polymer	f_d	N_p	N_d	$\phi_{eq}{}^a$	$L_{eq}{}^b$
HP38	0.2	480	240	0.130	45.13
HP38	0.3	420	360	0.293	34.42
HP38	0.4	360	480	0.333	32.99
HP38	0.5	300	600	0.293	34.41
HP38	0.6	240	720	0.246	36.47
HP38	0.7	180	840	0.164	41.76
MP38	0.2	480	240	0.164	41.74
MP38	0.3	420	360	0.305	33.94
MP38	0.4	360	480	0.333	32.98
MP38	0.5	300	600	0.297	34.25
MP38	0.6	240	720	0.249	36.34
MP38	0.7	180	840	0.162	41.88
HP19	0.4	720	480	0.319	33.44
HP76	0.4	180	480	0.328	33.14
MP19	0.4	720	480	0.324	32.27
MP76	0.4	180	480	0.332	33.00

[a] The volume fraction at the equilibrium swelling state.
[b] The length of a side of the simulation box at the equilibrium swelling state.

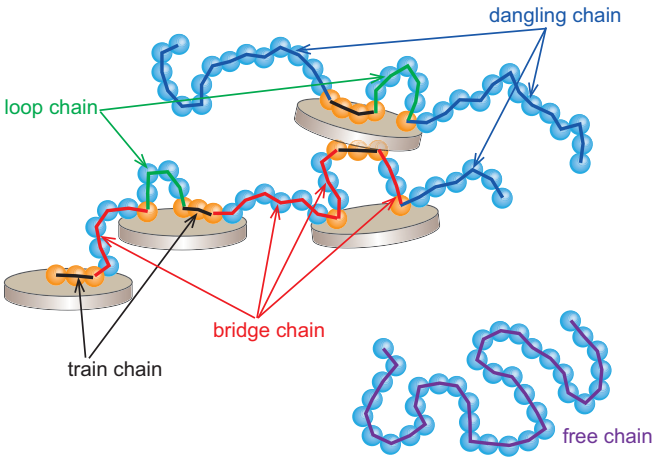

Figure S8 Five types of chain categories: bridge chain (red line), dangling chain (blue line), loop chain (green line), train chain (black line), and free chain (violet line). The orange spheres indicate the adsorbed beads.

In Figs. S10-S12, we show the effects of the polymer models on the relative populations of each chain category. At the relatively low composition ratios ($f_d \leq 0.3$), the sum of the relative populations of dangling chains and free chains decreases by the extension of the polymer length (HP19→HP38) or the introduction of the irreversible bonds between the polymer ends and the disk-shaped particles (HP38→MP38). These results mean that unadsorbed dangling ends decrease with increasing the irreversible bonds. At the low volume fraction ϕ and the low composition ratio f_d, the system including HP38s shows the increment of the relative populations of the free chains. However, since MP38s are grafted to the disk-shaped particles, the relative population of the free chains for MP38s does not increase within the range of $0.1 \leq f_d \leq 0.9$. Instead of the increment of the free chains, the relative population of the dangling chains for MP38s increases at the low volume fraction ϕ and the low composition ratio f_d. Therefore, the relative population of the dangling chains for MP38s is larger than that for HP38s at $f_d = 0.1$ in Fig. S10b. At the relatively high composition ratios ($f_d \geq 0.4$), where all beads belonging to the polymers can form the physical bonds with the disk-shaped particles and the effects of the dangling ends decrease, the differences between the polymer models reduce. These results are consistent with the results of the sol-gel transition concentration ϕ_{gel} and the equilibrium swelling ratio q_{eq} in the main text.

Evaluation of Equilibrium Swelling Ratio

To estimate the equilibrium swelling volume V_{eq} at which the stress σ_{diag} becomes 0, we carried out $1 \times 10^5 \tau_{LJ}$ simulation under a certain volume V and took the average over the later $5 \times 10^4 \tau_{LJ}$ as the result at V. We then plotted the stress σ_{diag} against the volume V and interpolated the stress σ_{diag} around the intersection with $\sigma_{diag} = 0$ (Fig. S13). We then defined the equilibrium swelling ratio as $q_{eq} \equiv V_{eq}/V_{dry}$. Here, V_{dry} is the volume corresponding to the molten state where the number density of beads is equal to 0.85 [1–3].

Figure S14 shows the volume fraction ϕ dependences of the percolation probability P and the sol fraction. At the volume fraction ϕ_{eq} of the equilibrium swelling state (Table S2), the percolation probability P is equal to 1, *i.e.*, the percolating cluster which can be regarded as an infinite network always exists during the simulation. The sol fraction is less than 0.03 at ϕ_{eq}. Furthermore, since the polymers form multiple physical bonds with the disk-shaped particles, the polymers are hardly desorbed from the disk-shaped particles. Therefore, we consider that the systems at the equilibrium swelling state form the stable networks.

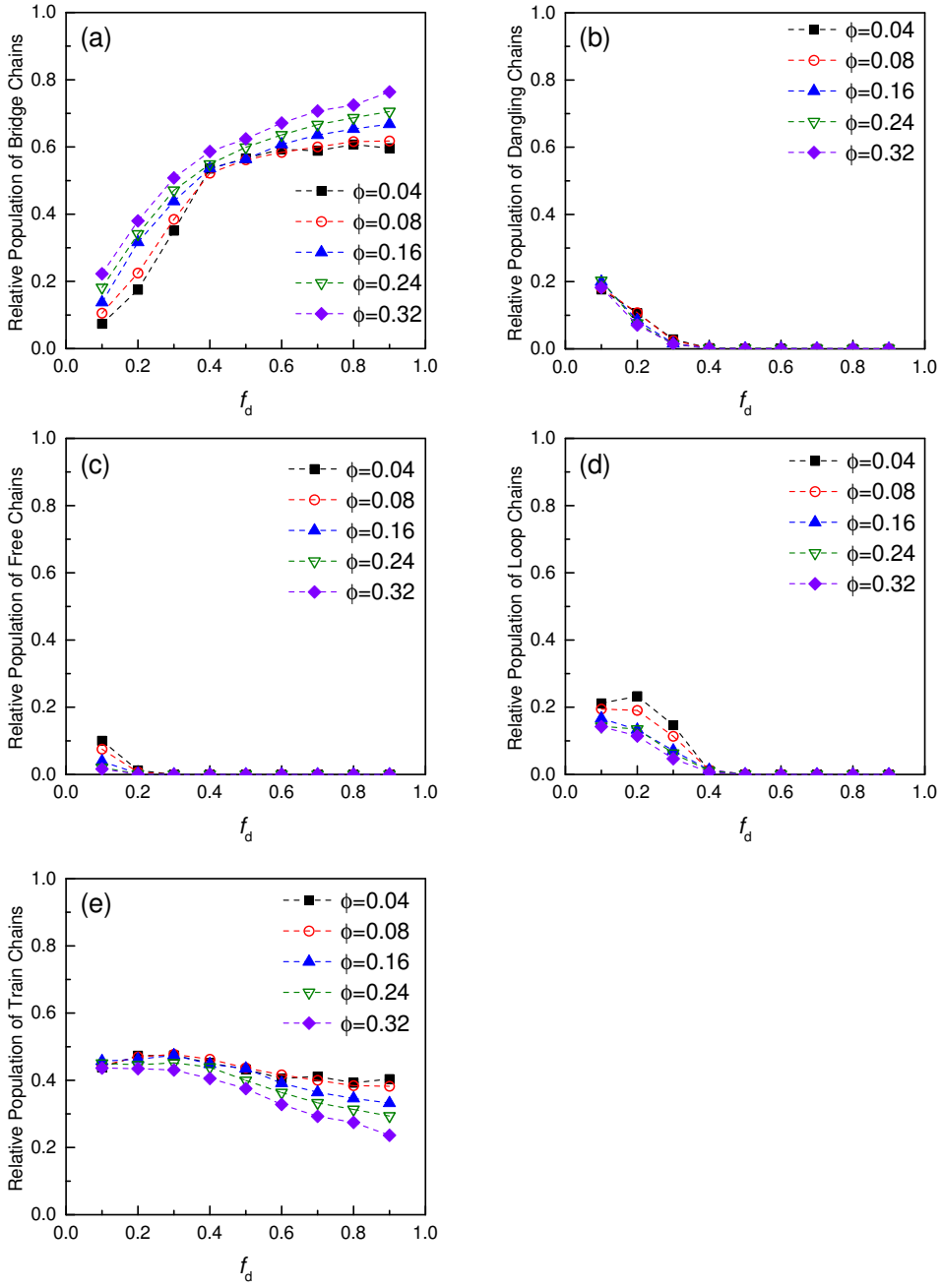

Figure S9 Relative populations of each chain category shown as functions of the composition ratio f_{d}: (a) bridge chains, (b) dangling chains, (c) free chains, (d) loop chains, and (e) train chains. The volume fraction ϕ is varied from data to data: $\phi = 0.04$ (■), $\phi = 0.08$ (◯), $\phi = 0.16$ (▲), $\phi = 0.24$ (▽), and $\phi = 0.32$ (♦). The polymer model is HP38.

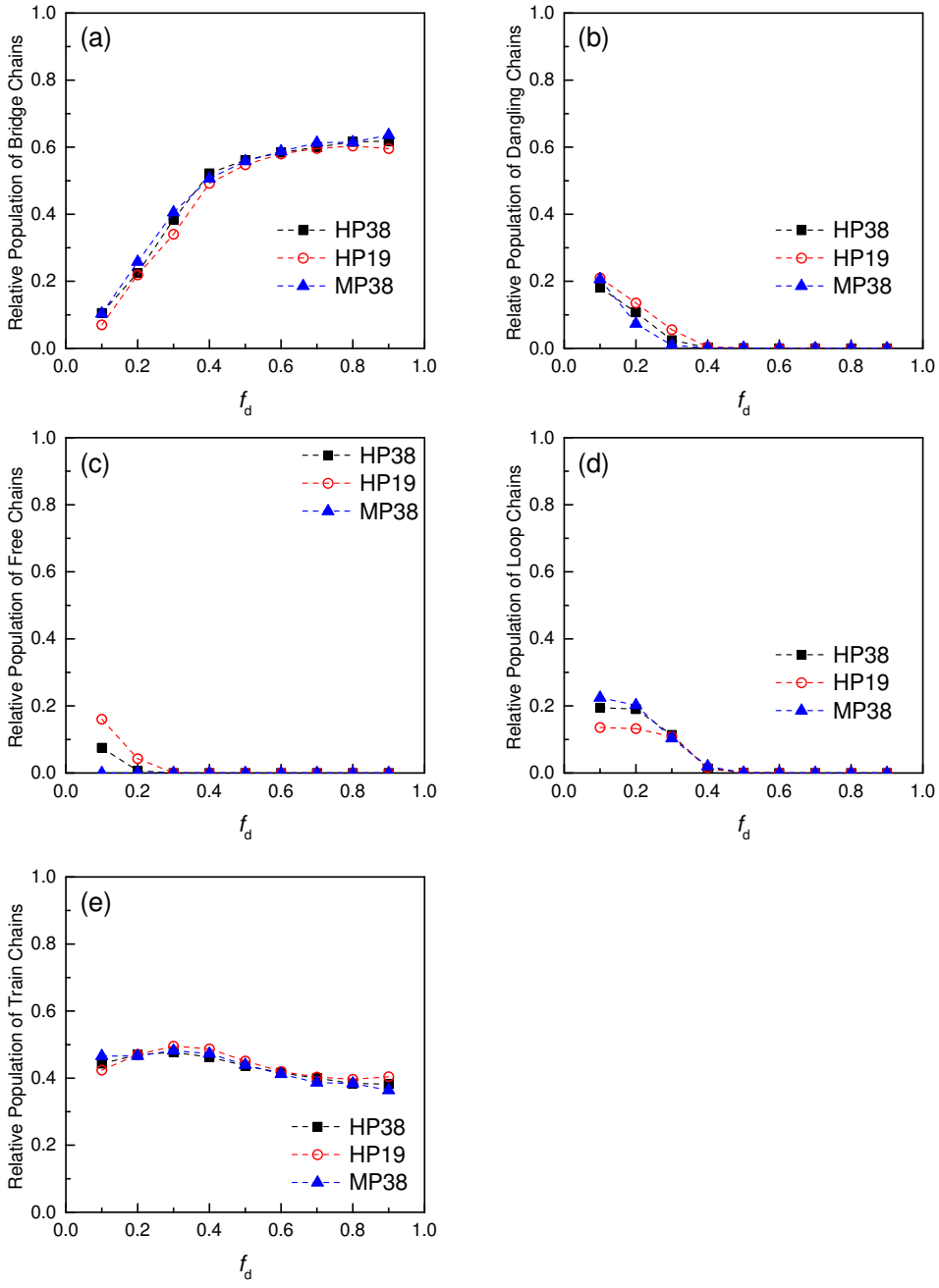

Figure S10 Relative populations of each chain category shown as functions of the composition ratio f_{d}: (a) bridge chains, (b) dangling chains, (c) free chains, (d) loop chains, and (e) train chains. The polymer model is varied from data to data: HP38 (■), HP19 (◯), and MP38 (▲). The volume fraction ϕ is fixed at $\phi = 0.08$.

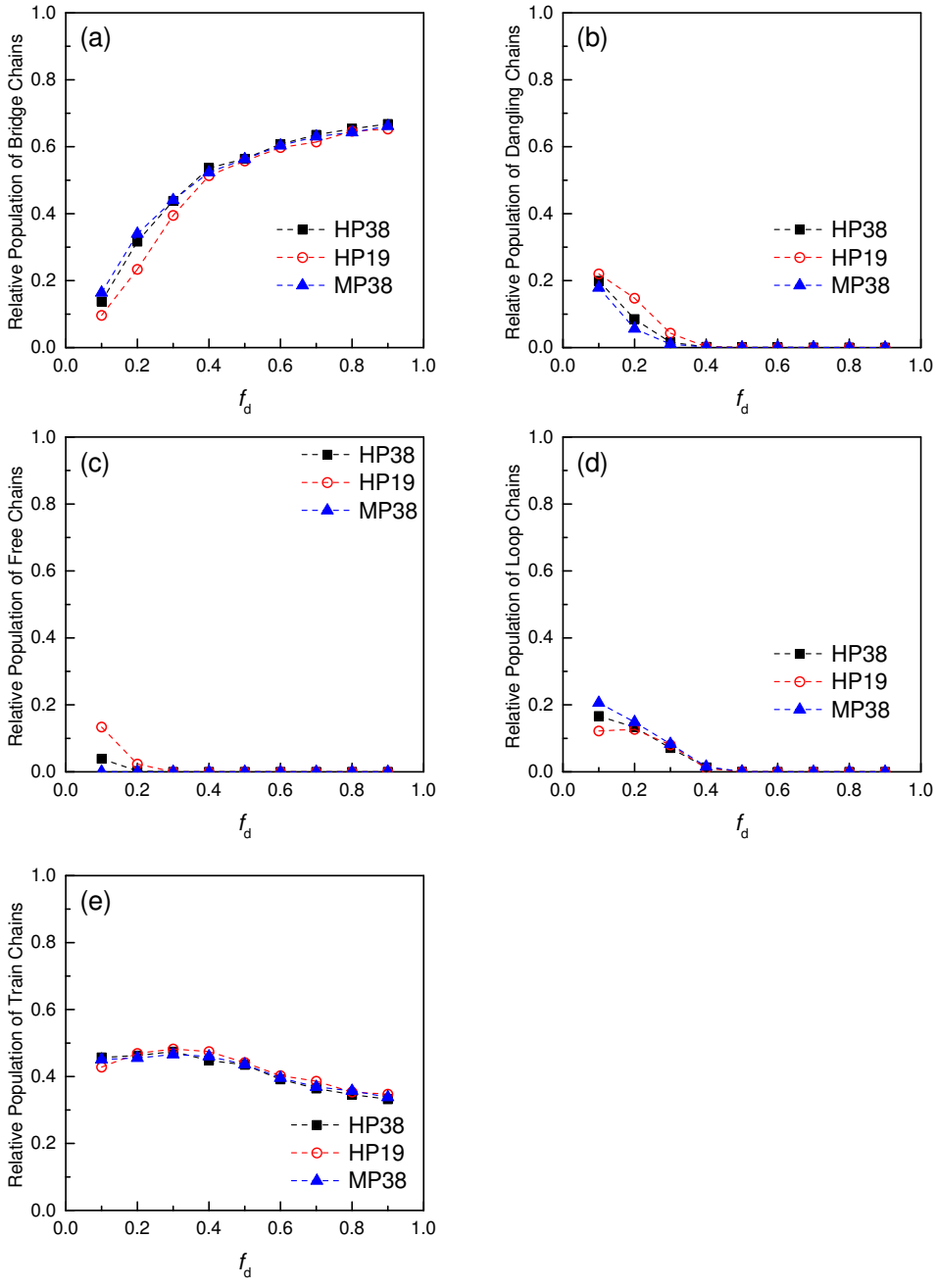

Figure S11 Relative populations of each chain category shown as functions of the composition ratio f_{d}: (a) bridge chains, (b) dangling chains, (c) free chains, (d) loop chains, and (e) train chains. The polymer model is varied from data to data: HP38 (■), HP19 (◯), and MP38 (▲). The volume fraction ϕ is fixed at $\phi = 0.16$.

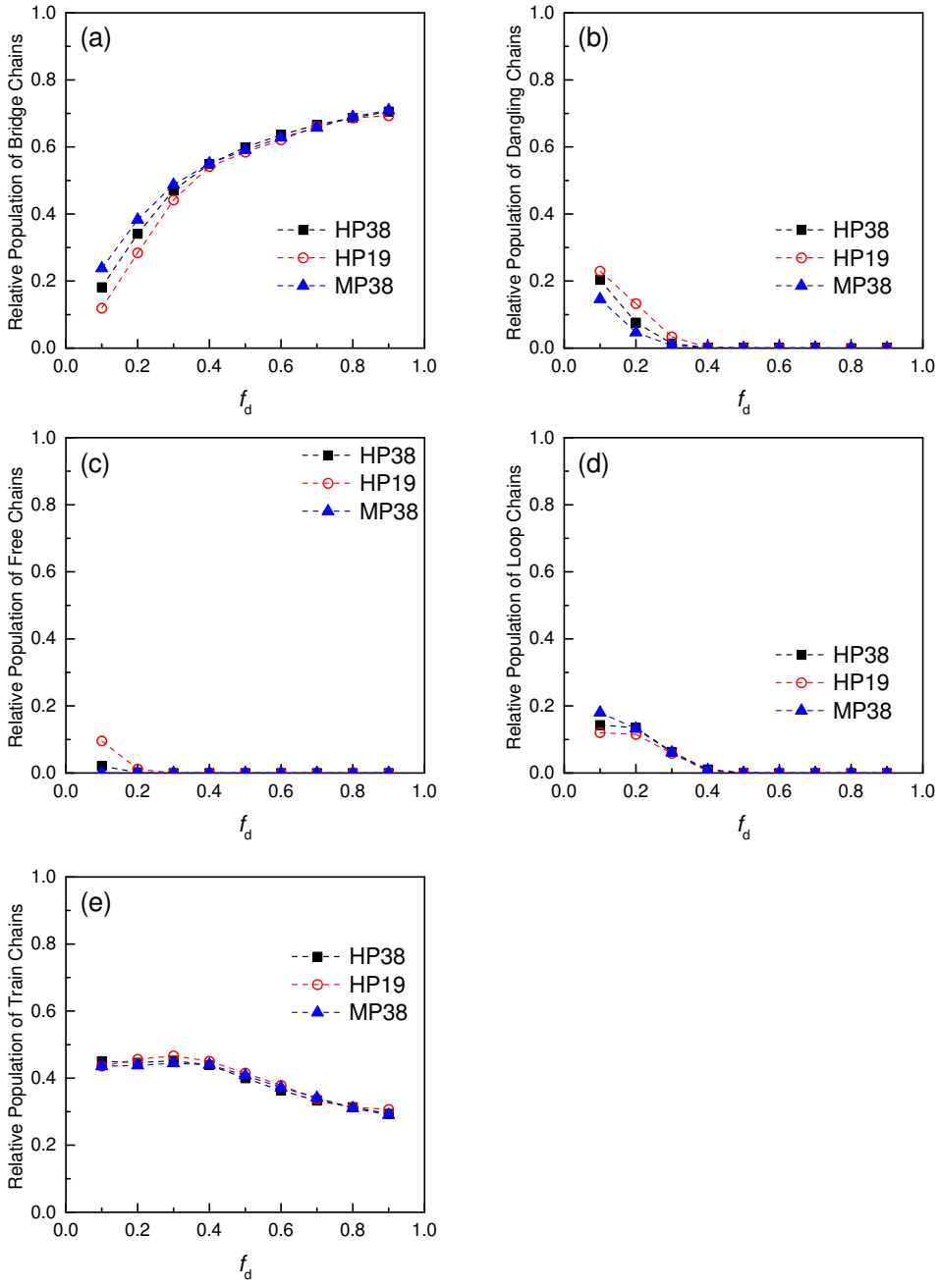

Figure S12 Relative populations of each chain category shown as functions of the composition ratio f_{d}: (a) bridge chains, (b) dangling chains, (c) free chains, (d) loop chains, and (e) train chains. The polymer model is varied from data to data: HP38 (■), HP19 (◯), and MP38 (▲). The volume fraction ϕ is fixed at $\phi = 0.24$.

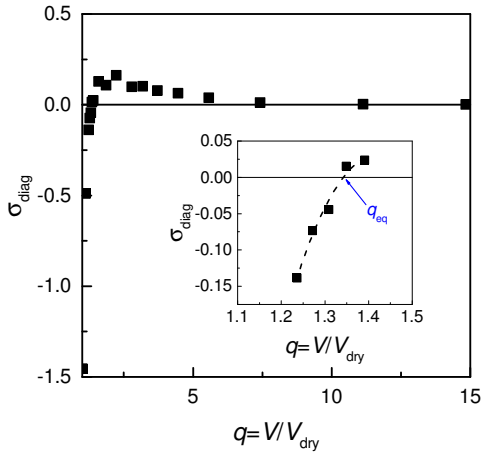

Figure S13 The swelling ratio $q = V/V_{\mathrm{dry}}$ dependence of the average of the diagonal components of the stress tensor σ_{diag}. The inset shows the results around the equilibrium swelling ratio $q_{\mathrm{eq}} = V_{\mathrm{eq}}/V_{\mathrm{dry}}$. The composition ratio f_{d} is fixed at $f_{\mathrm{d}} = 0.4$ and the polymer model is HP38.

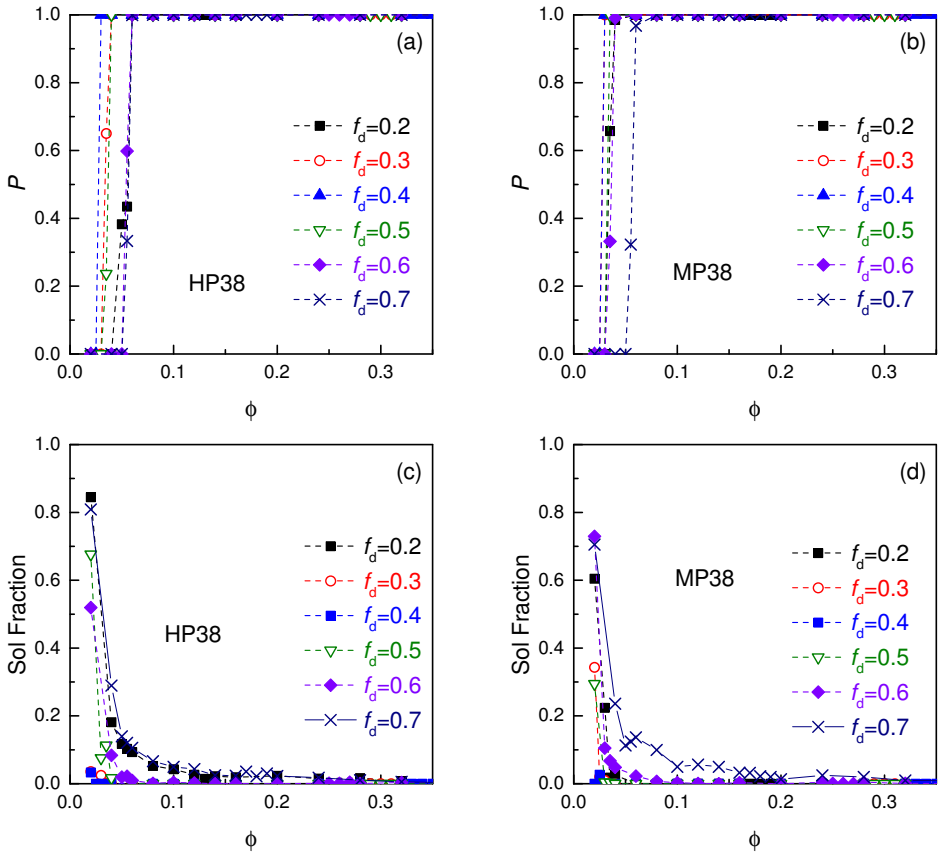

Figure S14 The percolation probability P shown as a function of the volume fraction ϕ for the polymer models (a) HP38 and (b) MP38. The sol fraction shown as a function of the volume fraction ϕ for the polymer models (c) HP38 and (d) MP38.

Evaluation of Elongation Ratio λ^*

We estimate the elongation ratio λ^* at which the slope of the elongation stress σ_{ue} changes from the point of intersection between the tangent line at $1 \leq \lambda \leq 1.2$ and that at $2 \leq \lambda \leq 2.5$ (Fig. S15a). Figure S15b shows the elongation ratio λ^* as a function of the number density $\nu_{b,eq}$ of the bridge chains at the equilibrium swelling state. As seen in Fig. S15b, the elongation ratio λ^* is almost independent of the polymer models and decreases with increasing the number density $\nu_{b,eq}$ of the bridge chains.

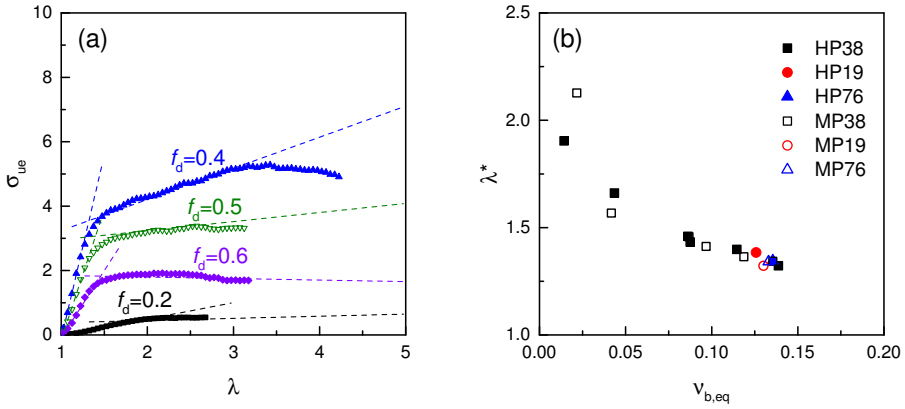

Figure S15 (a) The examples of the estimation method of the elongation ratio λ^*. (b) The elongation ratio λ^* shown as a function of the number density $\nu_{b,eq}$ of the bridge chains at the equilibrium swelling state.

Effects of Polymer Model on Network Structures

Figure S16 shows the weight average cluster size $\langle n_{cls} \rangle$ and the sol fraction for the networks consisting of MP38s and the disk-shaped particles as functions of the elongation ratio λ. Figures S17 shows the examples of the network structures at the equilibrium swelling state ($\lambda = 1$) and at the elongated state ($\lambda = 2$ and $\lambda = 4$). The results indicate the same behaviors as the results shown in Figs. 10 and 11 in the main text. The weight average cluster size n_{cls} rarely changes at the fracture elongation λ_f. Therefore, we find that the networks are fractured with one fracture surface. The weight average cluster size $\langle n_{cls} \rangle$ for $f_d = 0.7$ slightly increases before the fracture elongation λ_f and the sol fraction decreases. Hence, we think that the small clusters are incorporated in the network by the adsorption on the surfaces of the less dense region under this condition.

Figure S18 shows the average functionality $\langle g \rangle$ of the disk-shaped particles and the average number $\langle n_b \rangle$ of beads per bridge chain for the networks consisting of MP38s and the disk-shaped particles as functions of the elongation ratio λ. In Figs. S19 and S20, we present the effects of the number n_p of beads per polymer chain on the structures of the bridge chains. All of the polymer models show the same behavior. The average functionality $\langle g \rangle$ of the disk-shaped particles and the average number $\langle n_b \rangle$ of beads per bridge chains are almost constant at the small elongation ratios ($\lambda < \lambda^*$) where the stress sharply increases. At the large elongation ratios ($\lambda > \lambda^*$), the average functionality $\langle g \rangle$ of the disk-shaped particles decreases and the average number $\langle n_b \rangle$ of beads per bridge chains increases.

Orientations of Disk-shaped Particles and Polymers for Monofunctional Polymer Model

Figure S21 shows the results of the orientations of the disk-shaped particles and the polymers for the networks consisting of the disk-shaped particles and MP38s. The polymers are oriented in a direction parallel to the elongation direction and the normal vectors of the disk-shaped particles are oriented in a direction perpendicular to the elongation direction. The change rate $-\Delta C_d/\Delta\lambda$

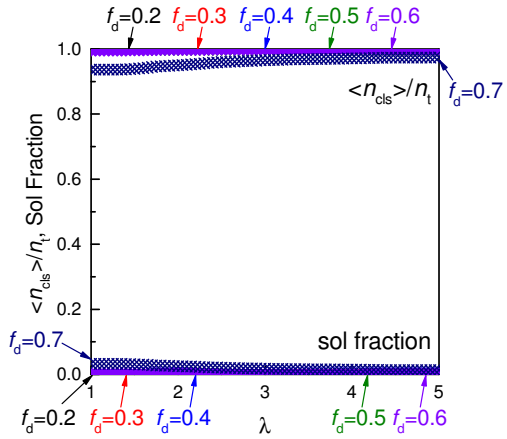

Figure S16 The weight average cluster size $\langle n_{\mathrm{cls}} \rangle$ and the sol fraction shown as functions of the elongation ratio λ. Here, n_{t} is the total number of beads. The composition ratio f_{d} is varied from data to data: $f_{\mathrm{d}} = 0.2$ (■), $f_{\mathrm{d}} = 0.3$ (◯), $f_{\mathrm{d}} = 0.4$ (▲), $f_{\mathrm{d}} = 0.5$ (▽), $f_{\mathrm{d}} = 0.6$ (♦), and $f_{\mathrm{d}} = 0.7$ (×). The polymer model is MP38.

approaches 0 more rapidly than $\Delta C_{\mathrm{p}}/\Delta\lambda$ at small elongation ratio. Therefore, the orientation of the disk-shaped particles saturates prior to the orientation of the whole polymer chains. These results of the orientations are the same as those of the networks including HP38s instead of MP38s.

Effects of Elongation Rate on Mechanical Properties

In order to study the effects of the elongation rate $\dot{\lambda}$ on the mechanical properties of the network, we performed the simulation with varying the elongation rate $\dot{\lambda}$. We here used the small systems of $n_{\mathrm{t}} = 5.7 \times 10^3$ and took the average over 12 independent runs. Figure S22 shows the elongation stress σ_{ue} as a function of the elongation ratio λ. The elongation stresses σ_{ue} for different elongation rates λ show the same trend; the elongation stresses σ_{ue} sharply increase with increasing the elongation ratio λ, decrease the slope, and then reach the fracture elongation λ_{f}. With decreasing the elongation rate $\dot{\lambda}$, the elongation stress σ_{ue} and the elongation ratio λ^* at which the slope of the elongation stress σ_{ue} changes decrease. The decreases of the elongation stress σ_{ue} and the elongation ratio λ^* are considered to be due to the restructuring of network structures via the recombination of the physical bonds. At the low elongation rate $\dot{\lambda}$, the total simulation time for the uniaxial elongation becomes comparable to the average lifetime τ_{a} of the physical bonds; hence, the influence of the recombination of the physical bonds increases. We think that the physical gel like properties of our simulation model are emphasized at the low elongation rates. Since we used the small systems in this section, the fracture elongation λ_{f} does not show clear dependence on the elongation rate $\dot{\lambda}$ (Table S3). To study the fracture elongation λ_{f}, it is necessary to calculate using the large system of $n_{\mathrm{t}} = 2.28 \times 10^4$.

Table S3 The fracture elongation λ_{f} with varying the elongation rate $\dot{\lambda}$.

polymer	f_{d}	$\dot{\lambda}$	λ_{f}
HP38	0.4	2×10^{-3}	4.4
HP38	0.4	1×10^{-3}	3.8
HP38	0.4	5×10^{-4}	4.1
HP38	0.4	2×10^{-4}	4.7
MP38	0.4	2×10^{-3}	> 5
MP38	0.4	1×10^{-3}	> 5
MP38	0.4	5×10^{-4}	> 5
MP38	0.4	2×10^{-4}	4.6

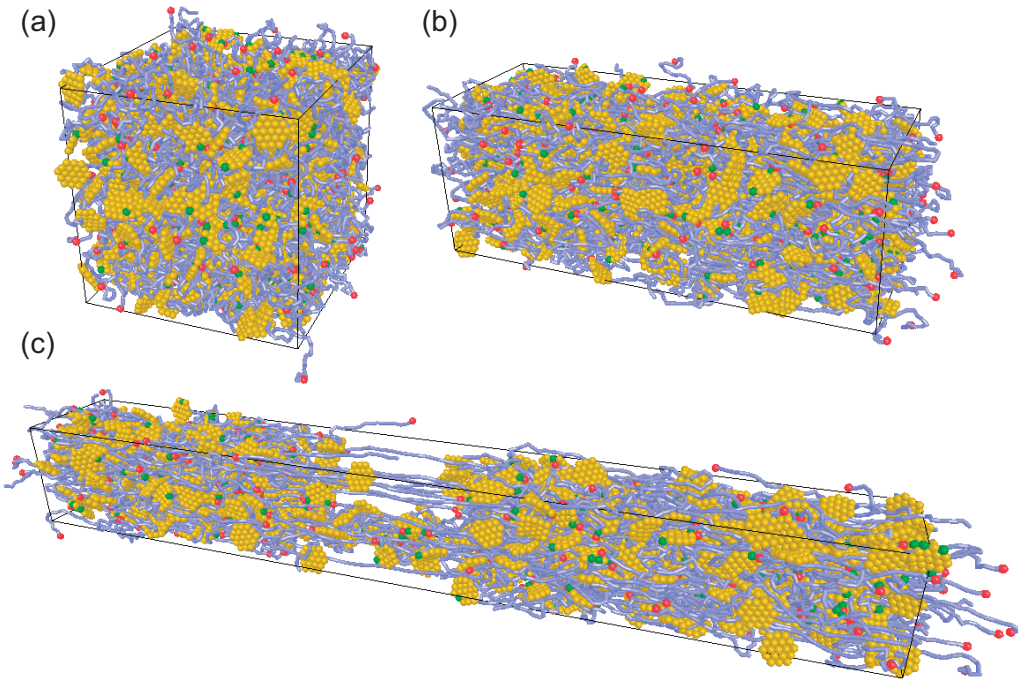

Figure S17 The network structures consisting of the MP38 polymers and the disk-shaped particles at (a) $\lambda = 1$, (b) $\lambda = 2$, and (c) $\lambda = 4$. The cylinders indicate the polymer bonds. The red, green, and yellow beads indicate the grafting beads of the MP38 polymers, the grafted beads of the disk-shaped particles, and other beads of the disk-shaped particles, respectively. The composition ratio f_{d} is $f_{\mathrm{d}} = 0.4$.

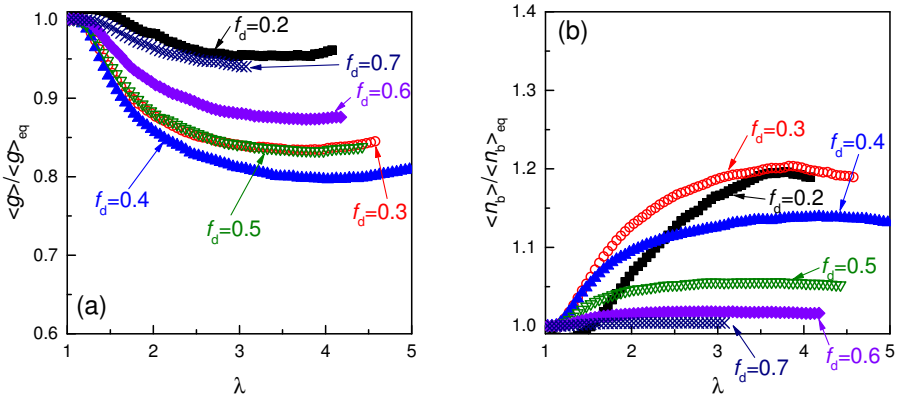

Figure S18 (a) The average functionality $\langle g \rangle$ of the disk-shaped particles and (b) the average number $\langle n_{\mathrm{b}} \rangle$ of beads per bridge chain shown as functions of the elongation ratio λ. The composition ratio f_{d} is varied from data to data: $f_{\mathrm{d}} = 0.2$ (■), $f_{\mathrm{d}} = 0.3$ (◯), $f_{\mathrm{d}} = 0.4$ (▲), $f_{\mathrm{d}} = 0.5$ (▽), $f_{\mathrm{d}} = 0.6$ (♦), and $f_{\mathrm{d}} = 0.7$ (×). The polymer model is MP38.

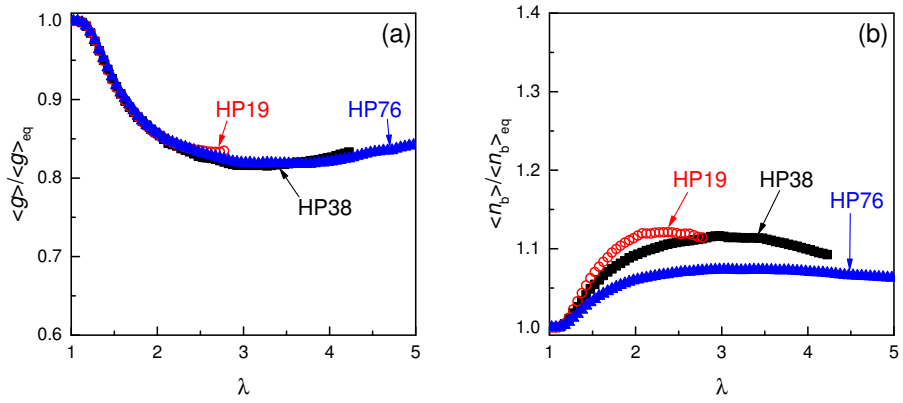

Figure S19 (a) The average functionality $\langle g \rangle$ of the disk-shaped particles and (b) the average number $\langle n_{\rm b} \rangle$ of beads per bridge chain shown as functions of the elongation ratio λ. The number $n_{\rm p}$ of beads per polymer is varied from data to data: $n_{\rm p} = 38$ (■), $n_{\rm p} = 19$ (◯), and $n_{\rm p} = 76$ (▲). The composition ratio $f_{\rm d}$ is $f_{\rm d} = 0.4$.

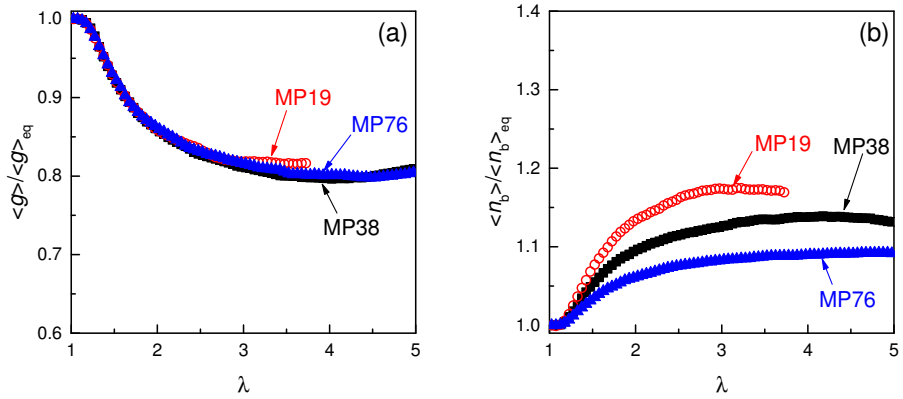

Figure S20 (a) The average functionality $\langle g \rangle$ of the disk-shaped particles and (b) the average number $\langle n_{\rm b} \rangle$ of beads per bridge chain shown as functions of the elongation ratio λ. The number $n_{\rm p}$ of beads per polymer is varied from data to data: $n_{\rm p} = 38$ (■), $n_{\rm p} = 19$ (◯), and $n_{\rm p} = 76$ (▲). The composition ratio $f_{\rm d}$ is $f_{\rm d} = 0.4$.

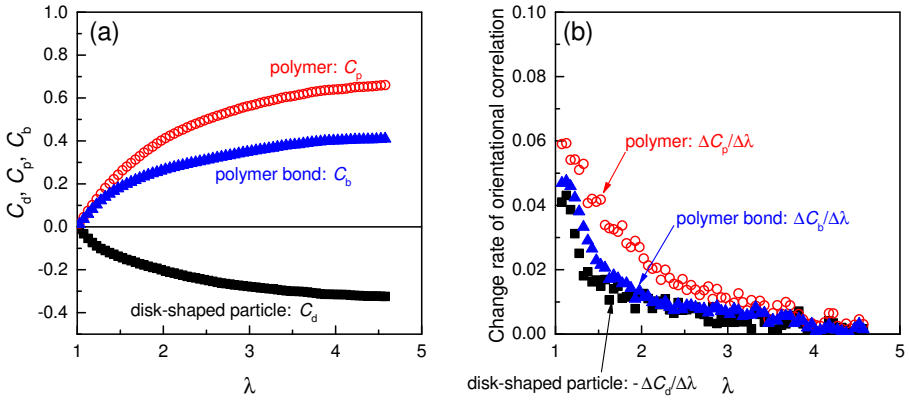

Figure S21 (a) The orientational correlation along the elongation direction of the normal vector of the disk-shaped particles (■), that of the end-to-end vector of the polymers (◯), and that of the polymeric bonds (▲) shown as functions of the elongation ratio λ. (b) The change rate of the orientational correlation of the disk-shaped particles (■), that of the polymers (◯), and that of polymeric bonds (▲) shown as functions of the elongation ratio λ. The polymer model is MP38 and the composition ratios $f_{\rm d}$ is $f_{\rm d} = 0.3$.

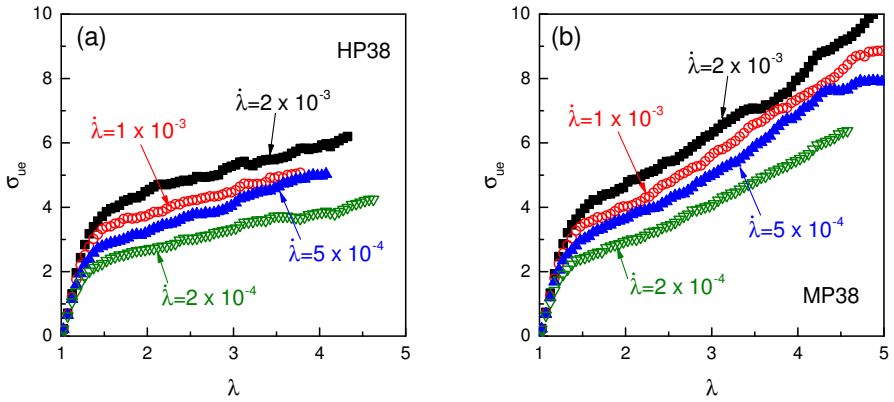

Figure S22 The stress-strain curves for the polymer models (a) HP38 and (b) MP38. The elongation rates $\dot{\lambda}$ is varied from data to data: $\dot{\lambda} = 2 \times 10^{-3} \tau_{\mathrm{LJ}}^{-1}$ (■), $\dot{\lambda} = 1 \times 10^{-3} \tau_{\mathrm{LJ}}^{-1}$ (◯), $\dot{\lambda} = 5 \times 10^{-4} \tau_{\mathrm{LJ}}^{-1}$ (▲), and $\dot{\lambda} = 2 \times 10^{-4} \tau_{\mathrm{LJ}}^{-1}$ (▽). The composition ratio f_{d} is fixed at $f_{\mathrm{d}} = 0.4$.

Cross-linked Polymer Network

In order to investigate the relationships between the network structures and the mechanical properties, we prepare the model network consisting of linear polymers and small cross-linkers. The linear polymer chain consists of $n_{\mathrm{p}} = 38$ beads and the cross-linker consists of one bead. This linear polymer chain is the same as the HP38 polymer in the main text. We assume that the cross-linker can form physical bonds with two polymer beads. If the networks are ideally formed, the cross-linkers act as four branch cross-linking points. We here employ the same potentials as that for the nanocomposite network: the LJ potential, the FENE potential, and the FENE-C potential.

We first placed N_{p} polymers and N_{c} cross-linkers at random in the cubic simulation box with periodic boundary conditions. After equilibration of $5 \times 10^4 \tau_{\mathrm{LJ}}$ calculation, we applied the uniaxial deformation in the same manner as the nanocomposite networks. We fixed the total number $n_{\mathrm{t}} \equiv n_{\mathrm{p}} N_{\mathrm{p}} + N_{\mathrm{c}}$ of beads at $n_{\mathrm{t}} = 5.7 \times 10^3$ and varied the composition ratio $f_{\mathrm{c}} \equiv N_{\mathrm{c}}/n_{\mathrm{t}}$ of the cross-linkers. The volume fraction ϕ was set to the volume fraction at the equilibrium swelling state of the corresponding nanocomposite network of $f_{\mathrm{d}} = f_{\mathrm{c}}$.

Table S4 shows the tensile modulus E and the characteristic values of the network structures. The functionalities $\langle g \rangle$ of the cross-linkers are smaller than those of the disk-shaped particles in the corresponding nanocomposite networks. The cross-linked polymer networks indicate smaller tensile moduli E than those of the nanocomposite networks. Due to the smaller functionalities $\langle g \rangle$ of the cross-linkers, a great number of bridge chains in the cross-linked polymer networks may be elastically ineffective. On the other hand, almost all of the bridge chains in the nanocomposite networks are considered to be elastically effective because of the high functionalities of the disk-shaped particles.

Table S4 The tensile modulus E and the characteristic values of the network structures of the cross-linked polymer networks.

f_{c}	E	$\langle g \rangle$	ν_{b}
0.2	0.05	2.35	0.058
0.3	0.70	3.18	0.267
0.4	0.70	2.54	0.323
0.5	0.24	1.69	0.236
0.6	0.09	1.10	0.155
0.7	0.01	0.68	0.074

References

[1] K. Kremer, G. S. Grest and I. Carmesin, *Phys. Rev. Lett.*, 1988, **61**, 566–569.

[2] K. Kremer and G. S. Grest, *J. Chem. Phys.*, 1990, **92**, 5057–5086.

[3] K. Kremer and G. S. Grest, *J. Chem. Soc., Faraday Trans.*, 1992, **88**, 1707–1717.